Remote Sens. **2012**, *4*, 1716-1740; doi:10.3390/rs4061716

OPEN ACCESS

Remote Sensing

ISSN 2072-4292

www.mdpi.com/journal/remotesensing

Article

Atmospheric Correction and Vicarious Calibration of Oceansat-1 Ocean Color Monitor (OCM) Data in Coastal Case 2 Waters

Padmanava Dash [1,*], Nan Walker [2], Deepak Mishra [3], Eurico D'Sa [2] and Sherwin Ladner [4]

[1] Department of Biology, Jackson State University, Jackson, MS 39217, USA

[2] Department of Oceanography and Coastal Sciences, Louisiana State University, Baton Rouge, LA 70803, USA; E-Mails: nwalker@lsu.edu (N.W.); ejdsa@lsu.edu (E.D.S.)

[3] Department of Geosciences, Northern Gulf Institute, and Geosystems Research Institute, Mississippi State University, Mississippi State, MS 39762, USA; E-Mail: dmishra@gri.msstate.edu

[4] Code 7331, Naval Research Laboratory, Stennis Space Center, MS 39529, USA; E-Mail: sherwin.ladner@nrlssc.navy.mil

***** Author to whom correspondence should be addressed; E-Mail: padmanava.dash@jsums.edu; Tel.: +1-601-979-3912; Fax: +1-601-979-5853.

Received: 26 April 2012; in revised form: 11 May 2012 / Accepted: 31 May 2012 / Published: 8 June 2012

Abstract: The Ocean Color Monitor (OCM) provides radiance measurements in eight visible and near-infrared bands, similar to the Sea-viewing Wide Field-of-View Sensor (SeaWiFS) but with higher spatial resolution. For small- to moderate-sized coastal lakes and estuaries, where the 1 × 1 km spatial resolution of SeaWiFS is inadequate, the OCM provides a good alternative because of its higher spatial resolution (240 × 360 m) and an exact repeat coverage of every two days. This paper describes a detailed step-by-step atmospheric correction procedure for OCM data applicable to coastal Case 2 waters. This development was necessary as accurate results could not be obtained for our Case 2 water study area in coastal Louisiana with OCM data by using existing atmospheric correction software packages. In addition, since OCM-retrieved radiances were abnormally low in the blue wavelength region, a vicarious calibration procedure was developed. The results of our combined vicarious calibration and atmospheric correction procedure for OCM data were compared with the results from the SeaWiFS Data Analysis System (SeaDAS) software package outputs for SeaWiFS and OCM data. For Case 1 waters, our results matched closely with SeaDAS results. For Case 2 waters, our results demonstrated closure with *in situ* radiometric measurements, while SeaDAS produced negative normalized water leaving radiance ($_nL_w$) and remote sensing reflectance (R_{rs}). In summary, our procedure

resulted in valid ${}_nL_w$ and R_{rs} values for Case 2 waters using OCM data, providing a reliable method for retrieving useful ${}_nL_w$ and R_{rs} values which can be used to develop ocean color algorithms for in-water substances (e.g., pigments, suspended sediments, chromophoric dissolved organic matter, *etc*.) at relatively high spatial resolution in regions where other software packages and sensors such as SeaWiFS and Moderate Resolution Imaging Spectrometer (MODIS) have proven unsuccessful. The method described here can be applied to other sensors such as OCM-2 or other Case 2 water areas.

Keywords: OCM; SeaWiFS; atmospheric correction; vicarious calibration; Case 2 water

Abbreviations

IRS	Indian Remote Sensing Satellite
ISRO	Indian Space Research Organisation
SeaWiFS	Sea-viewing Wide Field-of-View Sensor
MODIS	Moderate Resolution Imaging Spectroradiometer
MERIS	Medium Resolution Imaging Spectrometer
SeaDAS	SeaWiFS Data Analysis System
OCTS	Ocean Color and Temperature Scanner
CZCS	Coastal Zone Color Scanner
CDOM	Chromophoric Dissolved Organic Matter
FLAASH	Fast line-of-sight atmospheric analysis of spectral hypercubes
MLAC	Merged local area coverage
MOBY	Marine Optical Buoy
NASA	National Aeronautics and Space Agency
NRSC	National Remote Sensing Center
OBPG	Ocean Biology Processing Group
TOA	Top of the atmosphere
TOMS	Total Ozone Mapping Spectrometer
VIIRS	Visible Infrared Imager Radiometric Suite

1. Introduction

Satellite remote sensing provides a valuable tool for rapidly assessing the spatial variability of water quality parameters over synoptic scales [1]. However, use of satellite remote sensing for monitoring small lakes and estuaries is a challenge due to the optical complexities of these Case 2 water bodies leading to atmospheric correction problems ("Case 1" and "Case 2" defined in Morel and Prieur [2]). One such small lake is Lac des Allemands in Louisiana, USA, where high concentrations of cyanobacteria are known to occur in spring and summer [3–5].

Operational satellite monitoring of small water bodies requires higher spatial and temporal resolution [6]. The Oceansat-1 (IRS P-4) satellite launched on 26 May 1999 by the Indian Space

Research Organization (ISRO) carried the OCM sensor with spectral bands nearly identical to the SeaWiFS sensor. SeaWiFS and MODIS ocean bands have high radiometric sensitivity [7,8], however, they lack the spatial resolution needed for studying smaller water bodies. Other ocean color sensors that have the required spatial resolution for studying smaller water bodies, lack frequent revisit cycles. The Oceansat-1 OCM provides a compromise between the two types of sensors discussed above with a spatial resolution of 360 × 236 m and an exact revisit period of every alternate day.

OCM acquired data for a period of eleven years beginning in 1999, but these data have not been used extensively by the scientific community for studying Case 2 waters despite its higher spatial resolution. This is possibly due to one or more of the following: a lack of reliable atmospheric correction procedure and bio-optical algorithms for the sensor over Case 2 waters, the timing of its launch immediately following the launch of the long-awaited SeaWiFS instrument, and difficulty in data access by the scientific community [9]. This paper shows that it merits greater use. In addition, its successor, the OCM-2 sensor, was launched on 23 September 2009, and OCM-3 is planned for launch in 2013 [10]. With the recent failure of the SeaWiFS instrument, the OCM series of sensors provides a valuable alternative for ocean color data continuity, especially in coastal regions where other sensors experience atmospheric correction failure due to spatial resolution and optical complexity.

In ocean color remote sensing, the water-leaving radiance forms a small fraction of the total radiance received by the sensor, with the main contribution being due to the atmosphere. The NASA SeaWiFS Data Analysis System (SeaDAS) is one of the most comprehensive atmospheric correction programs used for processing ocean color data from several sensors including SeaWiFS, MODIS, OCTS, CZCS and MERIS. SeaWiFS and MODIS data processed by SeaDAS, over Case 1 waters, are widely used by the ocean color community. However, SeaDAS often fails to deliver the Case 1 type accuracy in shallow coastal Case 2 waters [6,11–13]. The SeaDAS atmospheric correction procedure assumes the water-leaving radiance to be negligible in the near infrared (NIR) which is one of the major reasons for its failure in Case 2 waters, because NIR reflectance is not zero in waters with high chlorophyll *a* and suspended sediments. Iterative approaches have been incorporated in SeaDAS software to correct for this problem [14–16]. However, due to the presence of even modest quantities of the constituents such as, suspended sediments or CDOM, which do not co-vary with chlorophyll *a*, SeaDAS processing fails in turbid coastal waters and either produces negative water-leaving radiances or masks the pixels.

Due to its small size and optical complexities, Lac des Allemands is often flagged and masked out in the SeaWiFS data processed through SeaDAS. OCM with its higher spatial resolution and SeaWiFS equivalent spectral bands is an appropriate sensor for the study of small lakes such as Lac des Allemands. However, unlike SeaDAS for SeaWiFS, OCM does not have a standard processing software package for atmospheric correction. Preliminary results showed that the existing data processing software including SeaSpace Terascan™, ENVI FLAASH, and SeaDAS did not yield valid ${}_nL_w$ in Lac des Allemands. Hence, there was a critical need for the development of an atmospheric correction procedure with the capability to process turbid Case 2 waters to utilize the full potential of OCM.

Hu *et al.* [11] developed a method of atmospheric correction for SeaWiFS data over turbid coastal waters by using the aerosol characteristics of a non-turbid adjacent region with an assumption that the type of aerosol does not vary much over relatively short spatial scales. They were able to retrieve realistic estimates of several in-water constituents from SeaWiFS turbid pixels, which had been flagged with either “negative water-leaving radiance” or “turbid water” flags in the SeaDAS processing.

SeaDAS enforces a rigorous atmospheric correction but, on the other hand, it is comprised of a complex suite of programs which is difficult to modify as a user. The principle of atmospheric correction for the ocean has been reviewed by Gordon [17], however in practice it is hard to find the solutions in one place [18], especially in the case of OCM. In this study, an atmospheric correction procedure was written for the processing of OCM data based on the extensive work done for SeaWiFS. The Hu *et al.* [11] aerosol correction technique has been incorporated in this procedure to increase the efficacy of the atmospheric correction over turbid-water pixels.

In addition to an accurate atmospheric correction procedure, a consistent vicarious calibration is also required to achieve the level of accuracy desired for quantitative oceanographic applications [19]. Amongst all the ocean color sensors, SeaWiFS had the most comprehensive vicarious calibration program in place [20] and it was continuously monitored for calibration errors using several direct methods and well-calibrated instruments such as one at the MOBY site near Hawaii [21–23]. As the OCM sensor has nearly identical bands and a similar equatorial crossing time to SeaWiFS, OCM data were vicariously calibrated using SeaWiFS data as reference.

In this study, an atmospheric correction procedure for OCM sensor was developed following that of SeaWiFS with the capability to accurately process Case 2 water bodies. In addition, a vicarious calibration procedure was developed and new coefficients were applied to the OCM data. The combined vicarious calibration and atmospheric correction procedure was implemented on OCM data at "clear-water" pixels and the results were compared with co-located SeaWiFS data processed with the same procedure and with the SeaDAS output. This procedure was then applied to the OCM data of Lac des Allemands and compared with field measurements and SeaDAS output. We demonstrated that valid normalized water-leaving radiances ($_nL_w$) and remote sensing reflectances (R_{rs}) could be retrieved over Case 2 waters using the combined vicarious calibration and atmospheric correction procedure developed in this study.

2. Materials and Methods

2.1. Satellite Data Processing Overview

OCM data were received via an X-band antenna and processed at the Earth Scan Laboratory, Louisiana State University. Raw OCM data were calibrated by converting raw counts to radiance values for the eight OCM spectral bands using the SeaSpace Terascan™ software. Six relatively clear-sky OCM images over the Gulf of Mexico were chosen from 2004 to 2007 (Table 1). SeaWiFS MLAC data of the same dates and similar overpass times (within 2 h of OCM overpass; 32 min to 1 h 42 min; Table 1) over the Gulf of Mexico were obtained from NASA's Ocean Color website (oceancolor.gsfc.nasa.gov) and processed through SeaDAS 6.0. Based on the OCM true color images (Figure 1) and the SeaWiFS derived chlorophyll *a* images (Figure 2), one "clear-water" (chlorophyll *a* conc. < 0.5 μg/L) site from the northern Gulf of Mexico was chosen in a clear-sky region in each of the SeaWiFS and OCM images. These clear water pixel sites are indicated as filled squares in the OCM true color and the SeaDAS processed SeaWiFS chlorophyll *a* images in Figures 1 and 2, respectively. Comparisons of OCM and SeaWiFS geometries and attributes at these six atmospheric correction sites on the six dates are given in Table 1.

To apply the Hu *et al.* [11] aerosol correction, six additional clear-water sites were chosen based on minimum TOA radiances in NIR bands 7 and 8 in the OCM and SeaWiFS images. The TOA radiance values in bands 7 and 8 were then corrected for Rayleigh path radiance for transferring the aerosol characteristics of these pixels to the corresponding atmospheric correction sites. The additional sites for aerosol correction are also shown in Figures 1 and 2. Atmospheric correction equations were then applied sequentially to the OCM TOA radiances to produce ${}_nL_w$ and R_{rs} before and after vicarious calibration. To compare the accuracy of the atmospheric correction procedure between OCM and SeaWiFS, ${}_nL_w$ and R_{rs} were produced in a similar fashion for SeaWiFS. Rayleigh and aerosol look up tables for OCM were generated (by B. Franz of OBPG, NASA) so that the OCM data could be processed through SeaDAS for comparison. The six SeaWiFS datasets were processed through both the single scattering and the default (multiple scattering) approaches in SeaDAS, which formed two more datasets. In summary, five datasets were generated including (1) OCM data processed with our atmospheric correction procedure (hereafter termed as 'new code'), (2) SeaWiFS data processed with the new code, (3) OCM data processed with SeaDAS, (4) SeaWiFS data processed with the SeaDAS single scattering approximation, and (5) SeaWiFS data processed with the SeaDAS multiple scattering approximation.

Table 1. Comparison of OCM and SeaWiFS attributes and geometries at the six atmospheric correction sites on the six dates.

Parameters	**OCM**	**SeaWiFS**	**OCM**	**SeaWiFS**	**OCM**	**SeaWiFS**
Date	5-Nov-04	5-Nov-04	7-Nov-04	7-Nov-04	19-Dec-04	19-Dec-04
Time of pixel scan (UTC)	18:05:43	18:55:33	18:06:05	18:38:46	18:05:47	19:09:18
Latitude	28.198	28.198	26.504	26.504	27.702	27.702
Longitude	−92.001	−92.001	−89.001	−89.001	−91.802	−91.802
Ozone Conc. (DU)	267	267	275	275	280	280
Satellite Zenith Angle	37.770	25.297	22.293	22.544	36.224	42.222
Solar Zenith Angle	44.847	46.786	44.047	45.372	51.031	53.455
Satellite Azimuth Angle	128.044	221.578	168.388	204.667	130.264	253.689
Solar Azimuth Angle	184.652	201.311	188.896	200.078	180.242	198.544
Sat_az-180-Sol_az	−236.608	−159.733	−200.507	−175.411	−229.977	−124.855
Relative Azimuth Angle	123.391	−159.733	159.492	−175.411	130.022	−124.855
Pressure	1,023.73	1,023.73	1,020.44	1,020.44	1,024.73	1,024.73
Parameters	**OCM**	**SeaWiFS**	**OCM**	**SeaWiFS**	**OCM**	**SeaWiFS**
Date	17-Nov-06	17-Nov-06	20-Apr-07	20-Apr-07	21-Jun-07	21-Jun-07
Time of pixel scan (UTC)	18:03:58	18:54:48	18:03:04	19:06:09	18:02:59	19:45:16
Latitude	27.099	27.099	28	28	27.54	27.54
Longitude	−92.1	−92.1	−91.001	−91.001	−90.55	−90.55
Ozone Conc. (DU)	278	278	286	286	301	301
Satellite Zenith Angle	37.110	41.733	32.523	31.258	30.426	49.963
Solar Zenith Angle	46.643	48.527	16.588	22.102	3.879	23.191
Satellite Azimuth Angle	129.368	125.144	135.770	140.678	142.916	260.344
Solar Azimuth Angle	183.151	199.511	179.826	225.2	178.569	265.533
Sat_az-180-Sol_az	−233.782	−254.367	−224.055	−264.522	−215.653	−185.189
Relative Azimuth Angle	126.217	105.633	135.944	95.478	144.346	174.811
Pressure	1,018.01	1,018.01	1,018.11	1,018.11	1,015.64	1,015.64

Figure 1. OCM true color images of northern Gulf of Mexico. The sites represented by filled squares are the clear water locations, where atmospheric correction was performed. The sites represented by filled triangles are the locations from where aerosol characteristics were transferred to the atmospheric correction sites.

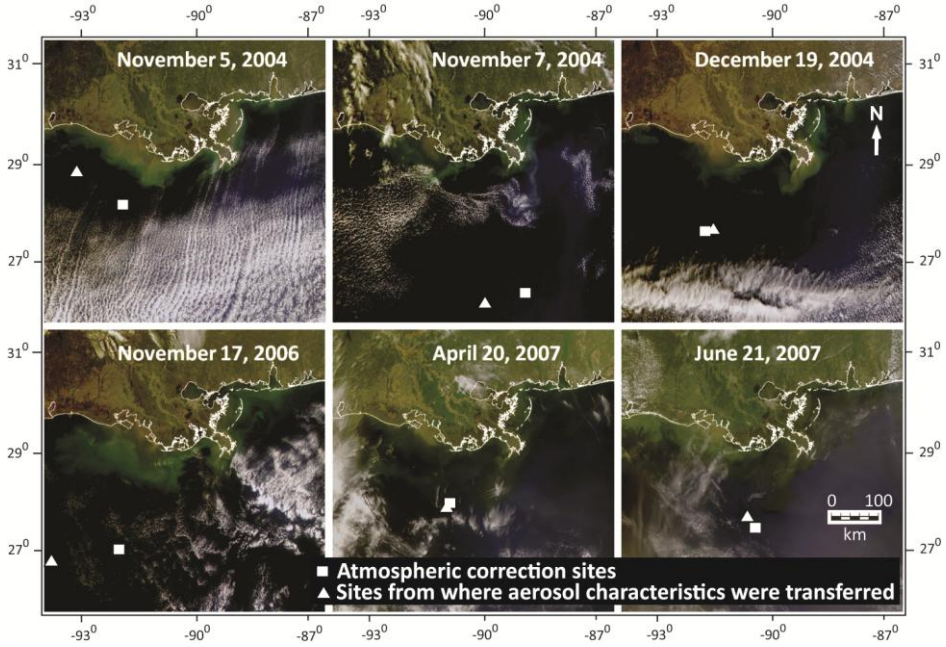

Figure 2. SeaDAS processed SeaWiFS chlorophyll *a* images of northern Gulf of Mexico. The sites represented by filled squares are the clear water locations, where atmospheric correction was performed. The sites represented by filled triangles are the locations from where aerosol characteristics were transferred to the atmospheric correction sites.

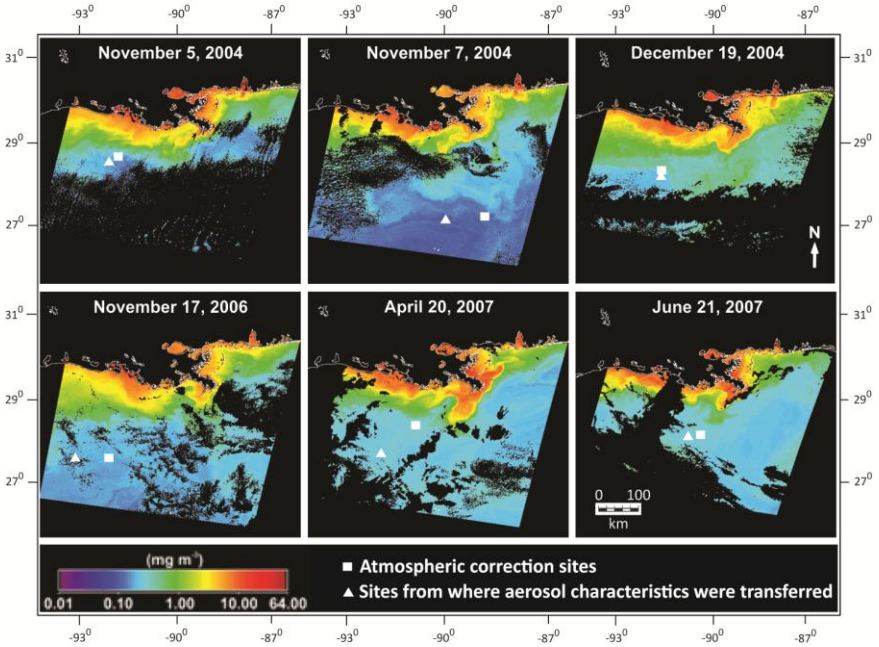

Finally, the new code was applied to the vicariously calibrated OCM data covering Lac des Allemands, located in the uppermost part of the Barataria estuary in southeastern Louisiana (Figure 3). Lac des Allemands is a freshwater lake (salinity < 1 psu) with a surface area of 49 km^2 and an average

depth of 2 m. The same OCM data were also processed through SeaDAS and the resulting ${}_nL_w$ values were compared to the OCM data processed through the new code. The new code results over Lac des Allemands were also compared to *in situ* radiometric measurements from a portable spectroradiometer (GER-1500, Geophysical & Environmental Research Corp., Poughkeepsie, NY, USA).

Figure 3. OCM image of 12 April 2007 showing the location of Lac des Allemands in southeastern Louisiana, with twelve sampling sites indicated [3].

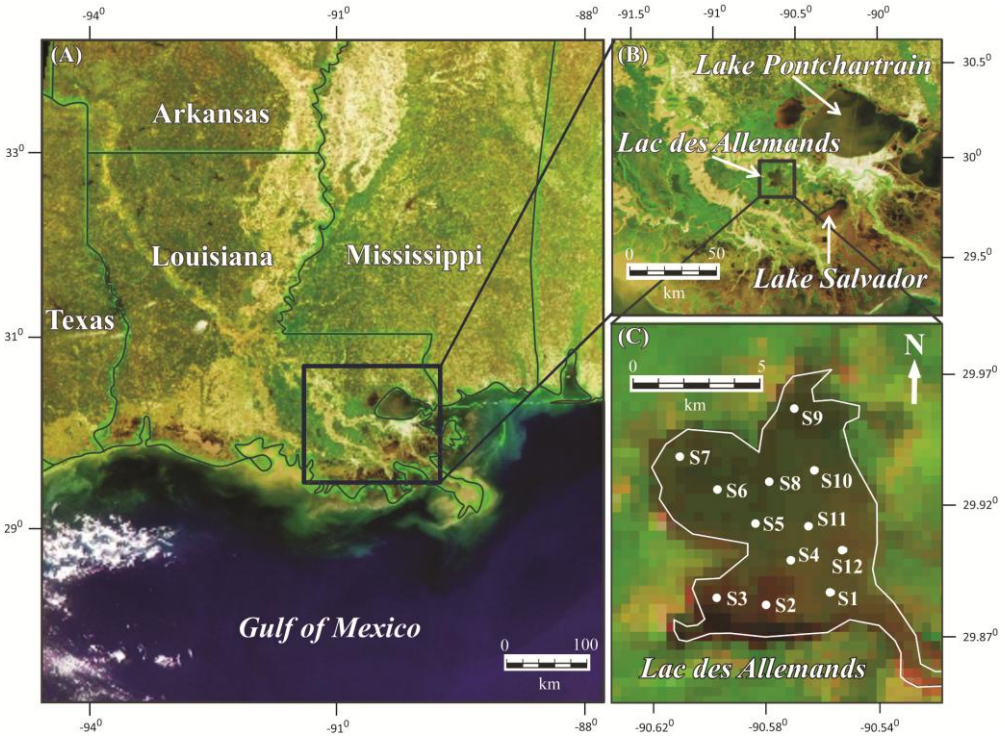

2.2. Atmospheric Correction Procedure

In a single scattering approach, the radiance received by a space borne sensor at the top of the atmosphere (TOA) in a spectral band centered at a wavelength, λ_i, $L_t(\lambda_i)$, can be divided into the following components [24,25]:

$$L_t(\lambda_i) = L_r(\lambda_i) + L_a(\lambda_i) + T(\lambda_i)L_g(\lambda_i) + t(\lambda_i)L_w(\lambda_i) \quad (1)$$

where $L_r(\lambda_i)$ and $L_a(\lambda_i)$ are radiance contributions associated with air molecules (Rayleigh scattering) and aerosols (including Rayleigh-aerosol interactions) respectively, T is the direct atmospheric transmittance, $L_g(\lambda_i)$ is the sun-glint component, t is the diffuse atmospheric transmittance, and $L_w(\lambda_i)$ is the desired water leaving radiance.

Sun-glint is usually avoided through tilting of the sensor. Hence, $T(\lambda_i)L_g(\lambda_i)$ may be ignored, and consequently, Equation (1) can be written as:

$$L_t(\lambda_i) = L_r(\lambda_i) + L_a(\lambda_i) + t(\lambda_i)L_w(\lambda_i) \quad (2)$$

First, contribution due to ozone absorption was removed from the TOA radiance as given by Hu *et al.* [18]:

$$L_t^*(\lambda_i) = L_t(\lambda_i) e^{\left[\tau_{oz}(\lambda_i)\left(\frac{1}{\cos\theta_0}+\frac{1}{\cos\theta_v}\right)\right]} \quad (3)$$

where $L_t^*(\lambda_i)$ is TOA radiance measured by the satellite in the absence of ozone, θ_v is satellite viewing zenith angle, θ_0 is solar zenith angle, and $\tau_{oz}(\lambda)$ is ozone optical depth, which was computed as [25,26]:

$$\tau_{oz}(\lambda_i) = k_{oz}(\lambda_i)\frac{DU}{1000} \quad (4)$$

where $k_{oz}(\lambda_i)$ is ozone absorption coefficient taken from Gregg and Carder [27] and DU is ozone concentration in Dobson units obtained from the TOMS website.

2.2.1. Computation of Rayleigh Path Radiance ($L_r(\lambda_i)$)

Rayleigh path radiance is the contribution of Rayleigh scattering by air molecules to TOA radiance. It was computed as given by Gordon [26]:

$$L_r(\lambda_i) = \frac{F_0'(\lambda_i)\omega_{0r}\tau_r(\lambda_i)P_r}{4\pi\cos\theta_v} \quad (5)$$

where $\tau_r(\lambda_i)$ is Rayleigh optical thickness, P_r is Rayleigh scattering phase function, ω_{0r} is single scattering albedo (equals to 1), and $F_0'(\lambda_i)$ is instantaneous extraterrestrial solar irradiance adjusted for the Sun-Earth distance as [18]:

$$F_0'(\lambda_i) = F_0(\lambda_i)/[1.00014 - 0.01671 \times \cos(2\pi(0.9856002831 \times \text{julianday} - 3.4532868)/360) - 0.00014 \times \cos(4\pi(0.9856002831 \times \text{julianday} - 3.4532868)/360)^2] \quad (6)$$

where $F_0(\lambda_i)$ is extraterrestrial solar irradiance. The $F_0(\lambda_i)$ values were adopted from Pandya *et al.* [28] for OCM and were converted to $mW \cdot cm^{-2} \cdot \mu m^{-1}$. The $F_0(\lambda_i)$ values for SeaWiFS data processing were adopted from SeaDAS.

Computation of Rayleigh Optical Thickness ($\tau_r(\lambda_i)$)

The value of Rayleigh optical thickness, $\tau_r(\lambda_i)$ at any atmospheric pressure P was calculated as given by Hansen and Travis [29]:

$$\tau_r(\lambda_i) = \frac{P}{P_0}[0.008569\lambda_i^{-4}(1+0.0113\lambda_i^{-2}+0.00013\lambda_i^{-4}) \quad (7)$$

where λ_i is wavelength in μm, and P_0 is standard atmospheric pressure of 1,013.25 mb.

Computation of Rayleigh Scattering Phase Function ($P_r(\theta_\pm)$)

The computations of Rayleigh scattering phase function involved the direct scattered light and the scattered light which is specularly reflected at the air-sea interface. It was computed as given by Doerffer [30]:

$$P_r(\theta_\pm) = \frac{3}{4}(1+\cos^2\theta_\pm) \quad (8)$$

where $\theta_\pm$ represents the scattering angles. The − and + subscripts indicate the direct scattered light and direct scattered plus the specularly reflected light at the air-sea interface, respectively. The scattering

angles in the direction to the sensor and in direction to the sensor via the air-sea interface is given by,

$$\cos\theta_{\pm} = \pm\cos\theta_0\cos\theta_v - \sin\theta_0\sin\theta_v\cos(\Delta\phi) \tag{9}$$

where $\Delta\phi$ represents the relative azimuth angle. Note that by definition the relative azimuth angle is the absolute difference between the satellite azimuth and the solar azimuth angles. In this definition the sun vector is considered in the down direction (sun to surface). However, it is a common practice (also instituted in SeaDAS) to define both the sun vector and the sensor vector in the upward direction [31] and thus the relative azimuth angle was obtained as:

$$\Delta\phi = \phi_v - 180 - \phi_0 \tag{10}$$

where ϕ_0 and ϕ_v are solar and satellite azimuth angles, respectively. Further, to keep the values between $\pm 180°$, $360°$ was added or subtracted when the relative azimuth angles were less than $-180°$ and greater than $180°$, respectively.

At the air-sea interface, another phenomenon occurs with the specularly reflected light that should be accounted for in the computation of Rayleigh phase function is Fresnel reflection. It is the reflection that occurs when light propagates through media with different refractive indices. As none of the relevant media (air or water) are magnetic, when the light is polarized with the electric field of the light perpendicular to the incident light (s-polarized), the Fresnel reflection coefficient is calculated as:

$$\mathrm{R}(\theta_i)_s = \sin^2(\theta_i - \theta_j) / \sin^2(\theta_i + \theta_j) \tag{11}$$

where θ_i is solar zenith angle (θ_0) for R(θ_0) and satellite viewing zenith angle (θ_v) for R(θ_v) calculation, and θ_j is determined through Snell's law as:

$$\sin(\theta_i) / \sin(\theta_j) = n = 1.333 = \text{refractive index of water} \tag{12}$$

When the light is polarized in the same plane as the incident light (p-polarized), the Fresnel reflection coefficient is calculated by:

$$\mathrm{R}(\theta_i)_p = \tan^2(\theta_i - \theta_j) / \tan^2(\theta_i + \theta_j) \tag{13}$$

Assuming the incident light contains an equal mix of s- and p-polarizations, the Fresnel reflection coefficient was computed as [17]:

$$\mathrm{R}(\theta_i) = 0.5[\mathrm{R}(\theta_i)_s + \mathrm{R}(\theta_i)_p] \tag{14}$$

The total Rayleigh scattering phase function was computed as given by Doerffer [30] and Gordon and Wang [32]:

$$\mathrm{P_r}(\theta_{\pm}) = \mathrm{P_r}(\theta_-) + [\mathrm{R}(\theta_v) + \mathrm{R}(\theta_0)]\mathrm{P_r}(\theta_+) \tag{15}$$

where $\mathrm{P_r}(\theta_{\pm})$ is total Rayleigh scattering phase function, $\mathrm{P_r}(\theta_-)$ is Rayleigh scattering phase function when solar radiation is directly backscattered to the sensor, and $\mathrm{P_r}(\theta_+)$ is Rayleigh scattering phase function due to the specularly reflected light at the air/sea interface in addition to the direct backscattered light.

2.2.2. Computation of Aerosol Path radiance ($L_a(\lambda_i)$)

Aerosol path radiance is the contribution of scattering by particles similar to or larger than the wavelength of light such as dust, pollen, smoke or water vapor in the atmosphere to the TOA radiance.

Unlike L_r, which can be computed fairly accurately, L_a is difficult to determine since the aerosol scattering is highly variable and many times there is no a priori information on their optical properties and size distributions. By using the sensor radiances above 700 nm, it is possible to determine L_a indirectly [32]. Over Case 1 clear-waters, water-leaving radiance is negligible in the NIR bands because of strong NIR absorption by water, thus, the radiance measured is essentially the contributions from the atmosphere. Therefore, L_a can be estimated after removing L_r from the TOA radiance at the NIR bands. To estimate L_a in the visible wavelengths, (two NIR bands are required): one NIR band for assessing the magnitude of aerosol's contribution and another for assessing its dependence on wavelength. The Gordon and Wang [32] atmospheric correction algorithm uses the SeaWiFS NIR band centered at 865 nm to estimate the aerosol scattering and 765 nm band together with 865 nm band to extrapolate into visible.

The technique described above does not work over Case 2 waters because NIR reflectance is influenced by the optically active constituents in the water. Therefore in this study, the Hu *et al.* [11] aerosol correction procedure was used for an accurate correction of aerosol scattering. A clear-water pixel close to the atmospheric correction site was identified in the same scene from the open ocean waters where the TOA radiances at the NIR bands were minimal. L_a at the two NIR bands was determined after removing L_r from the TOA radiance. From L_a at the two NIR bands, L_a for bands less than 700 nm were computed through extrapolation using a spectral model following Gordon and Wang [32], Gordon *et al.* [17], and Mohan and Chauhan [33]. The expression for aerosol path radiance [30] is:

$$L_a(\lambda_i) = \frac{F_0'(\lambda_i)\omega_{0a}\tau_a P_a}{4\pi \cos\theta_v} \tag{16}$$

where ω_{0a} is single scattering albedo (equals to 1), τ_a is aerosol optical thickness, and P_a is aerosol scattering phase function. By assuming an exponential relationship between aerosol optical thickness and wavelength [32], $\tau_a \propto e^{\lambda}$, and the phase function to remain constant over the desired wavelengths [33], Equation (16) can be modified to:

$$L_a(\lambda) / F_0'(\lambda) = ke^{(-c\lambda)} \tag{17}$$

where k and c are constants. Natural logarithm in both sides of Equation (17) leads to:

$$Ln[L_a(\lambda) / F_0'(\lambda)] = k\ (-c)\ \lambda = -\varepsilon\lambda \tag{18}$$

$Ln[L_a(\lambda)/F_0'(\lambda)]$ for OCM NIR bands centered at 768.6 and 865.1 nm were plotted against λ, and ε was determined as the negative of the slope of the straight line as:

$$\frac{Ln\left\{L_a(\lambda_{865.1}) / F_0'(\lambda_{865.1})\right\} - Ln\left\{L_a(\lambda_{768.6}) / F_0'(\lambda_{768.6})\right\}}{\lambda_{865.1} - \lambda_{768.6}} = -\ \varepsilon \tag{19}$$

Once ε was known, the L_a for the wavelengths below 700 nm were determined as:

$$L_a(\lambda_i < 700nm) = L_a(\lambda_{865.1})(F_0' / F_0'(\lambda_{865.1}))e^{[-\varepsilon(\lambda_i / \lambda_{865.1})]} \tag{20}$$

2.2.3. Computation of Diffuse Transmittance ($t(\lambda_i)$)

Diffuse transmittance from the water surface to the satellite was computed as [18]:

$$t(\lambda_i) = e^{\left[-\left(\frac{\tau r(\lambda_i)}{2}\right)\left(\frac{1}{\cos\theta_v}\right)\right]} \tag{21}$$

2.2.4. Computation of Water-Leaving Radiance ($L_w(\lambda_i)$)

The desirable water-leaving radiance at a specific wavelength was computed by rewriting the Equation (2) as:

$$L_w(\lambda_i) = \frac{L_t^*(\lambda_i) - L_r(\lambda_i) - L_a(\lambda_i)}{t(\lambda_i)} \tag{22}$$

2.2.5. Computation of Normalized Water-Leaving Radiance ($_nL_w(\lambda_i)$)

The $_nL_w$ is approximately the radiance that would exit the ocean in the absence of atmosphere with sun at the zenith at mean earth-sun distance (1 AU), and was computed as given by Gordon and Voss [34]:

$$_nL_w(\lambda_i) = \frac{L_w(\lambda_i)}{d^{-2} \times \cos\theta_0 \times e^{\left\{-\left(\frac{\tau r(\lambda_i)}{2}\right)\left(\frac{1}{\cos\theta_0}\right)\right\}}} \tag{23}$$

where d is earth-sun distance in astronomical unit (AU).

2.2.6. Computation of Remote Sensing Reflectance ($R_{rs}(\lambda_i)$)

The R_{rs} associated with $_nL_w$ was computed as given by Gordon and Voss [34]:

$$R_{rs}(\lambda_i) = \frac{_nL_w(\lambda_i)}{F_0(\lambda_i)} \tag{24}$$

This atmospheric correction procedure does not include out-of-band correction, whitecap correction, surface roughness influences and contribution of L_a to diffuse transmittance. However, these corrections will not significantly change the overall accuracy of the procedure particularly for small lakes or estuaries on low wind speed days when whitecap and surface roughness terms are minimal.

2.3. *Vicarious Calibration*

In addition to an accurate atmospheric correction, a precise vicarious calibration is crucial to the success of any quantitative ocean color remote sensing data retrieval because of the uncertainties associated with pre-launch calibration coefficients [19]. Therefore, post-launch vicarious calibration of ocean color sensors in a timely manner is necessary. Any systematic bias associated with the atmospheric correction algorithm further emphasizes the need to continuously monitor all the bands for any calibration errors. Thus, the vicarious calibration as discussed below is the procedure to determine new coefficients for adjustments of the TOA radiance due to both, post launch changes in sensor response, and any unknown bias due to the atmospheric correction algorithm.

Vicarious calibration is usually achieved by comparing satellite-derived $_nL_w$ and *in situ* measured $_nL_w$, but it can also be based on models, regional climatology data or retrievals from other sensors [19]. In the absence of any "ground" truth such as buoy or other suitable matchup data, an inter-comparison of satellite sensors is often the best choice [23]. As the SeaWiFS instrument was well-calibrated, the

SeaWiFS ${}_nL_w$ values are the best choice to vicariously calibrate another satellite sensor, particularly when the bands of the sensor to be calibrated (e.g., OCM) are nearly identical to SeaWiFS and the sensor has a similar overpass time as SeaWiFS. The OCM calibration table was last updated in 2003 [35]. Therefore, OCM data processed using the old calibration table produced abnormal ${}_nL_w$ values during preliminary analysis. Thus, the OCM bands were vicariously calibrated using coincident and co-located SeaWiFS data. SeaWiFS images were processed through SeaDAS 6.0. OCM data were navigated and registered by overlaying the coastline by visually matching with the corresponding SeaDAS processed SeaWiFS images. ${}_nL_w$ values at the six sites were extracted and compared with the corresponding OCM ${}_nL_w$ radiance data produced through our atmospheric correction procedure. Since the atmospheric contribution to TOA radiance can be safely assumed constant for three adjacent OCM pixels (which are nearly equivalent to the size of one SeaWiFS pixel) over open ocean waters and there is no difference in the optical properties of clear water, a pixel-to-pixel comparison between OCM and SeaWiFS was considered accurate. Out of the eight OCM bands, the two NIR bands were not considered for vicarious calibration due to near-zero NIR water-leaving radiance in clear water areas. Based on the comparison, six calibration coefficients were determined for OCM bands 1–6 using an optimization technique and multiplied to corresponding OCM TOA radiance such that the combined root mean square error (RMSE) for all the six dates between OCM and SeaWiFS ${}_nL_w$ was minimal. Thus, for the vicarious calibration coefficient for the band *i*, the RMSE for the *i* th band, e_i was computed as:

$$e_i = \sqrt{\frac{\sum_{j=1}^{n}\left\{(OCM\_{}_nL_{w_{ij}}) - (SeaWiFS\_{}_nL_{w_{ij}})\right\}^2}{n}} \tag{25}$$

where *i* represents OCM bands from 1 to 6, and *j* represents overpass days from 1 to 6.

Table 2. Vicarious calibration coefficients of OCM bands 1–6.

Bands	Wavelength (nm)	Vicarious Calibration Coefficients	Error in Original TOA Radiance
Band 1	404–424 (414.2)	1.162430130338560	16.2%
Band 2	432–452 (441.4)	1.099317412022420	9.93%
Band 3	479–499 (485.7)	1.097377164249840	9.73%
Band 4	502–522 (510.6)	1.093961431616450	9.39%
Band 5	547–567 (556.4)	1.085434622452900	8.54%
Band 6	660–680 (669.0)	1.021605349340930	2.16%

The vicarious calibration coefficients are presented in Table 2. As these coefficients were computed for various observation dates over the OCM lifespan, they can be termed as OCM mission mean vicarious gains and could be used to produce more accurate OCM TOA radiances. Originally, SeaWiFS data are vicariously calibrated by comparing SeaWiFS TOA radiances with the predicted TOA radiances from the ${}_nL_w$ obtained at the MOBY site so that the average difference between the MOBY and SeaWiFS ${}_nL_w$ are minimal. In our vicarious calibration procedure, we used SeaWiFS ${}_nL_w$ values as a proxy for *in situ* ${}_nL_w$ and compared these with ${}_nL_w$ from co-located pixels of OCM data. We used an optimization technique to correctly predict the TOA radiances from the OCM data using the new atmospheric correction procedure. Therefore, our vicarious calibration coefficients adjust for any changes in the response due to the atmospheric correction procedure, in addition to the changes due to

instrument bias or any other source of calibration error. Since, this is a simple and straight-forward approach, new calibration coefficients can be computed easily when needed in future.

2.4. Destriping

After atmospheric correction of vicariously calibrated OCM data, occasional abnormalities were observed in the spectral shapes of the retrieved OCM R_{rs}, especially in bands 1, 2 and 3. For example, sometimes a peak was observed at OCM band centered at 441.4 nm. If these abnormalities were due to calibration error, this typical low-high-low shape corresponding to OCM bands 1, 2 and 3 should have appeared in the spectra of all the stations on the same day. From comparison with 250 m resolution MODIS-Aqua images, we observed that MODIS-Aqua bands do not have these periodic features, meaning that the OCM features are artifacts. After analyzing several images carefully, we concluded that these artifacts in OCM data were due to striping. Upon registration and geolocation, these along-track stripes result in image speckling. Lyon [36] developed an Automated Destriping algorithM (ADM) to remove the effects of striping from OCM data. ADM has been integrated into the Automated Processing System (APS) of Naval Research Laboratory, Stennis Space Center, Mississippi, USA. The OCM images over Lac des Allemands were destriped using ADM before vicarious calibration and atmospheric correction.

In situ R_{rs} values were obtained with a hand-held GER 1500 radiometer on selected dates at the 12 sites in Lac des Allemands coinciding with clear-sky OCM data. The hyperspectral radiometer data were weighted with the relative spectral response function of OCM to yield R_{rs} values at the six OCM bands. Weighted radiometer R_{rs} and R_{rs} estimated by the new code before and after destriping were compared to gauge the performance of the combined destriping, vicarious calibration and atmospheric correction approach.

3. Results and Discussion

The following datasets were compared and analyzed for the six study sites: (a) new code processed OCM data [New code OCM], (b) new code processed SeaWiFS data [New code SeaWiFS], (c) SeaDAS processed SeaWiFS data with multiple scattering approximations [SeaDAS (default) SeaWiFS], (d) SeaDAS processed SeaWiFS data with single scattering approximations [SeaDAS (single scattering) SeaWiFS] and (e) SeaDAS processed OCM data [SeaDAS OCM].

In most instances, L_r is much greater than all the other atmospheric attenuation components, so it is critical that the computations of L_r be carried out accurately [37]. To assess the accuracy of L_r estimation, the new code computed L_r were compared with SeaDAS provided L_r along OCM and SeaWiFS scan lines (Figures 4 and 5). It is well-known that L_r values increase from the scene center towards the edges with the increase in satellite zenith angles forming a U-shaped curve, which is particularly noticeable in the blue bands. For the SeaWiFS scene, the new code computed L_r and SeaDAS provided L_r were consistent with each other for the most part except for the scan edges of the blue bands (Figure 5). These differences in L_r at SeaWiFS scan edges were due to the high swath width of SeaWiFS. However for the entire OCM scene, the new code computed L_r were in good agreement with SeaDAS provided L_r (Figure 4).

Figure 4. Comparison of Rayleigh path radiance for OCM bands 1–6 calculated by the new code and SeaDAS along a scan line of OCM data of 21 June 2007.

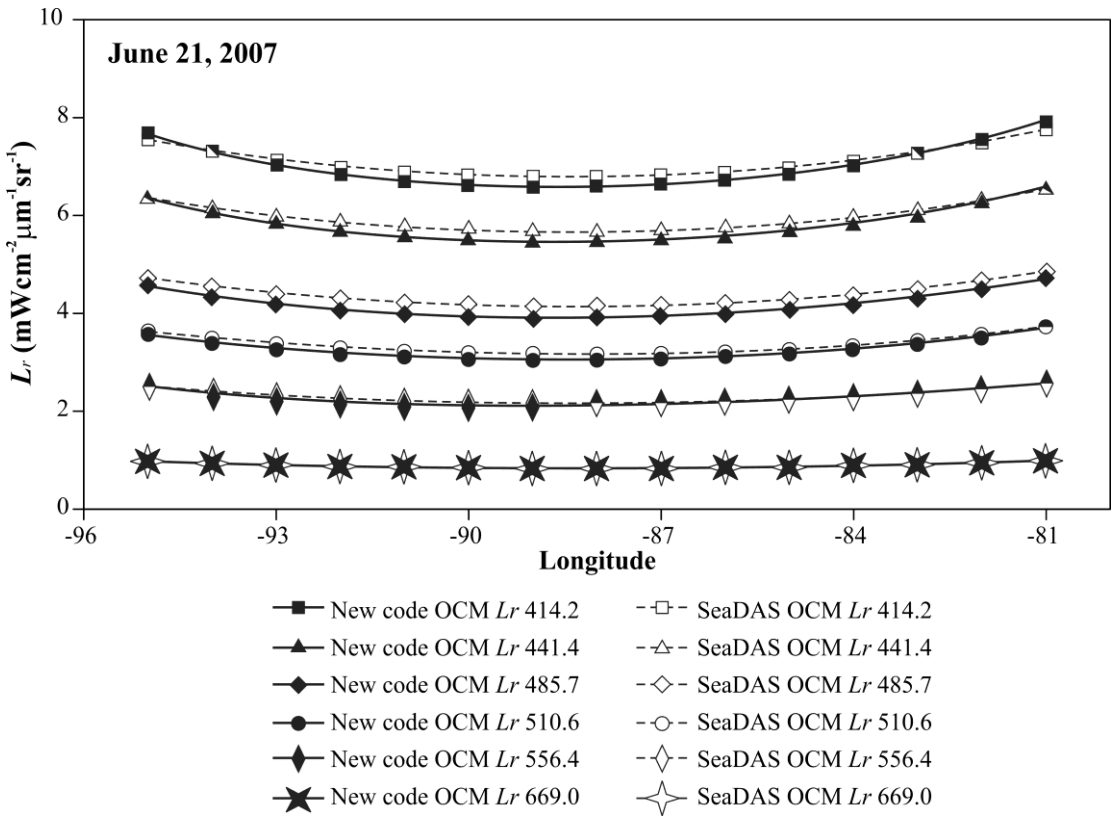

Figure 5. Comparison of Rayleigh path radiance for SeaWiFS bands 1–6 calculated by the new code and SeaDAS along a scan line of SeaWiFS data of 21 June 2007.

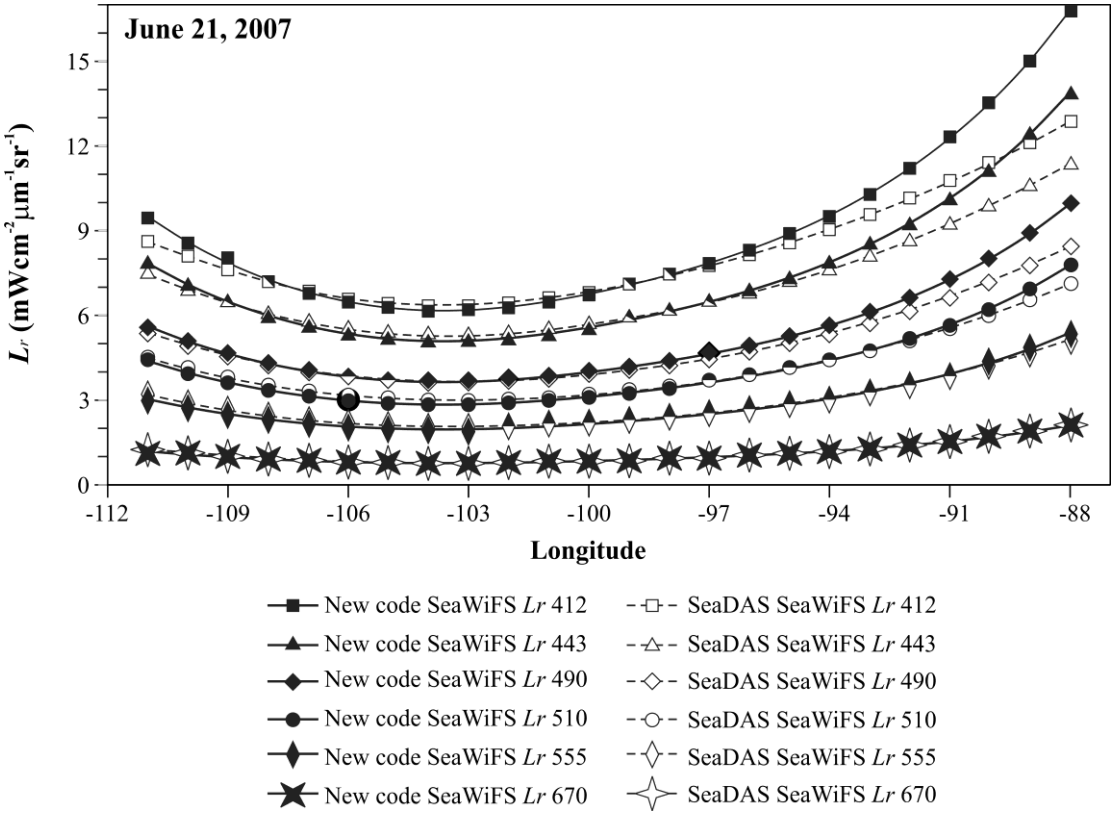

For a range of τ_r values, sun angles, and viewing angles of interest, L_r calculated with the single scattering approximations can differ from the results of scalar radiative transfer models by 3–4 percent, and the L_r computed by scalar radiative transfer models can differ from vector radiative transfer models (models including polarization by approximately the same amount) by a few percent [37,38]. Our procedure uses a single scattering approximation for computations of L_r, but it incorporates corrections for polarization, by considering approximately equal s- and p-polarizations. The SeaDAS atmospheric correction algorithm uses lookup tables for Rayleigh and aerosol radiances, which are generated with over ~25,000 radiative transfer simulations using multiple scattering approximations. SeaDAS does not provide single scattering L_r, therefore, single scattering comparison of new code computed L_r and SeaDAS provided L_r was not possible. However, SeaDAS can provide single scattering L_a; therefore, single and multiple aerosol scattering provided by SeaDAS can be compared. It was found that sometimes small differences existed in SeaDAS produced single and multiple aerosol scattering approximations (not shown). We found that the new code computed L_r values were fairly accurate with a difference of less than 5% from SeaDAS computed L_r. Thus, we concluded that, by employing the new code, a reasonable correction for L_r could be accomplished.

Figure 6 shows the comparison of Rayleigh radiance, aerosol radiance and diffuse transmittance calculated by the new code and SeaDAS over the atmospheric correction sites for the OCM data. L_r computed by the new code and SeaDAS were in good agreement for the dates 7 November 2004, 20 April 2007 and 21 June 2007. Since Rayleigh scattering depends on solar and viewing geometries and the location of the observation site within the scene, the differences were greater between the new code and SeaDAS computed L_r on 5 November 2004, 19 December 2004 and 17 November 2006. The new code derived diffuse transmittance and aerosol radiance values for all the sites and dates were in agreement with the SeaDAS calculations (Figure 6).

Figure 6. Comparison of Rayleigh path radiance (L_r), aerosol path radiance (L_a) and Diffuse transmittance (t) calculated by the new code and SeaDAS at the atmospheric correction sites in each of the OCM data.

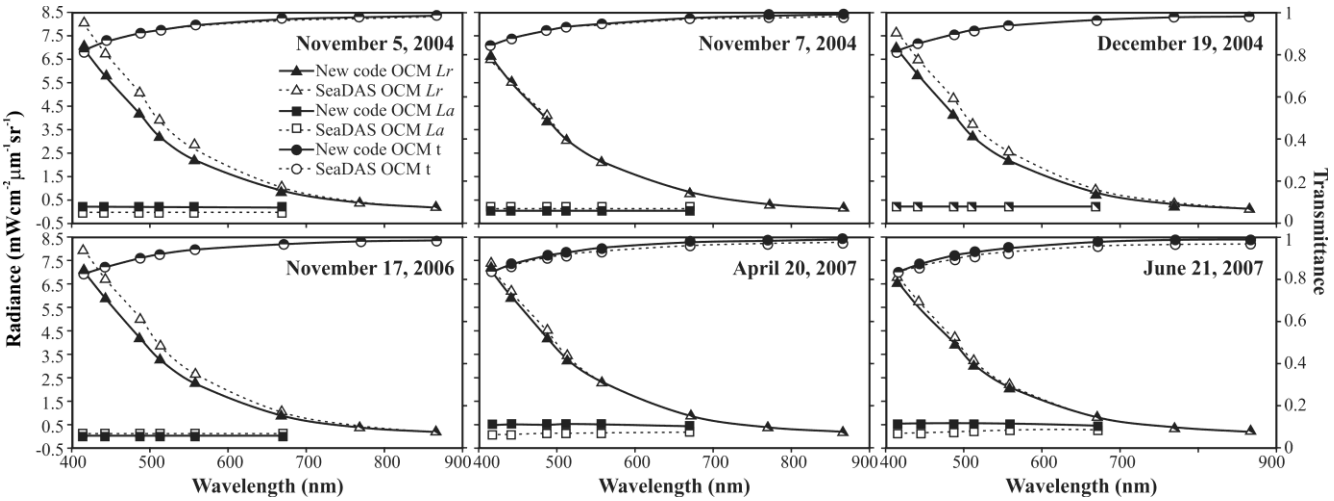

OCM data of 19 December 2004 had stripes in band 1, but other bands were stripe free. Unfortunately, the atmospheric correction site for 19 December 2004 was on a stripe with bad data, which prevented L_a, L_w, ${}_nL_w$, and R_{rs} calculations for any band from SeaDAS processing. Therefore,

SeaDAS processed L_a is not shown for 19 December 2004 in Figure 6. Although a destriping algorithm such as the one proposed by Lyon [36] (used in this paper) or Wang and Franz [12] could be applied to eliminate this type of striping artifact, the atmospheric correction procedure should not transfer the effects of stripes to other bands, as occurs in the SeaDAS processing. However, the new code deals with each band individually. Therefore, the observed striping in band 1 on 19 December 2004 did not negatively impact data retrieval in other bands.

Figure 7 compares the OCM TOA radiances before and after vicarious calibration, and the corresponding ${}_nL_w$ values computed by the new code and SeaDAS. Before vicarious calibration significant errors were observed especially in the blue bands (Figure 7, Table 2). Large calibration errors resulted in low TOA radiances. Since the atmospheric correction terms are computed independently, upon applying these corrections to the lower than anticipated TOA radiance, negative ${}_nL_w$ values were obtained before vicarious calibration. Note that for 19 December 2004, the SeaDAS processed ${}_nL_w$ were not available as the site was on a stripe of bad data. Before vicarious calibration the shapes of ${}_nL_w$ spectra did not resemble expected clear-water spectral shapes. After vicarious calibration, OCM ${}_nL_w$ values were positive even in the blue bands and resembled clear-water spectral shapes [39]. The new code and SeaDAS processed spectra were in good agreement. The vicarious calibration procedure presented in this study is similar to the SeaWiFS procedure. SeaWiFS vicarious calibration computes the coefficients by predicting TOA radiance after matching SeaWiFS ${}_nL_w$ values with the MOBY ${}_nL_w$ values. Our vicarious calibration computes the coefficients by predicting TOA radiance after matching OCM ${}_nL_w$ values with near synchronous SeaWiFS ${}_nL_w$ values. This procedure also adjusts the deviations resulting from integrated instrument and atmospheric correction. Therefore, if OCM data are vicariously calibrated using the coefficients given in Table 2 and processed with the atmospheric correction procedure presented in this study, the resulting ${}_nL_w$ values will be in agreement with SeaWiFS ${}_nL_w$ values of the same dates. In addition, this simple procedure can be easily duplicated and these calibration coefficients can be updated for the OCM data of any date irrespective of the calibration status of OCM data. This procedure can also be used to derive vicarious calibration coefficients for other ocean color sensors.

Figure 8 shows the comparisons between the new code and SeaDAS processed SeaWiFS, and vicariously calibrated OCM ${}_nL_w$ spectra. The spectral shapes of SeaDAS processed SeaWiFS (with the default multi-scattering and the single scattering approaches) were similar with a slight difference in magnitude. The new code processed SeaWiFS ${}_nL_w$ values were in good agreements with SeaDAS processed SeaWiFS ${}_nL_w$ values, however, a difference was observed in the first few bands. This is because the SeaWiFS data were not vicariously calibrated when processed through the new code. In SeaDAS, the SeaWiFS vicarious calibration coefficients of the corresponding dates are usually applied prior to atmospheric correction using look-up-tables within SeaDAS. If the SeaWiFS data are not processed through SeaDAS, the vicarious calibration coefficients are not being applied automatically and differences in radiance values would be observed. From Figure 8, it is clear that the blue SeaWiFS bands were most affected by these calibration errors. Hu *et al.* [11] also found significantly lower water-leaving radiances in SeaWiFS bands 1 and 2 while processing SeaWiFS data through their modified atmospheric correction procedure. They also attributed this to incorrect calibrations in the SeaWiFS bands 1 and 2.

Figure 7. Comparison of OCM TOA radiances before and after vicarious calibration, and the corresponding ${}_nL_w$ values computed by the new code and SeaDAS. Solid dots with solid lines represent vicariously calibrated ${}_nL_w$ and TOA radiances, and hollow dots with dotted lines represent ${}_nL_w$ and TOA radiances before vicarious calibration.

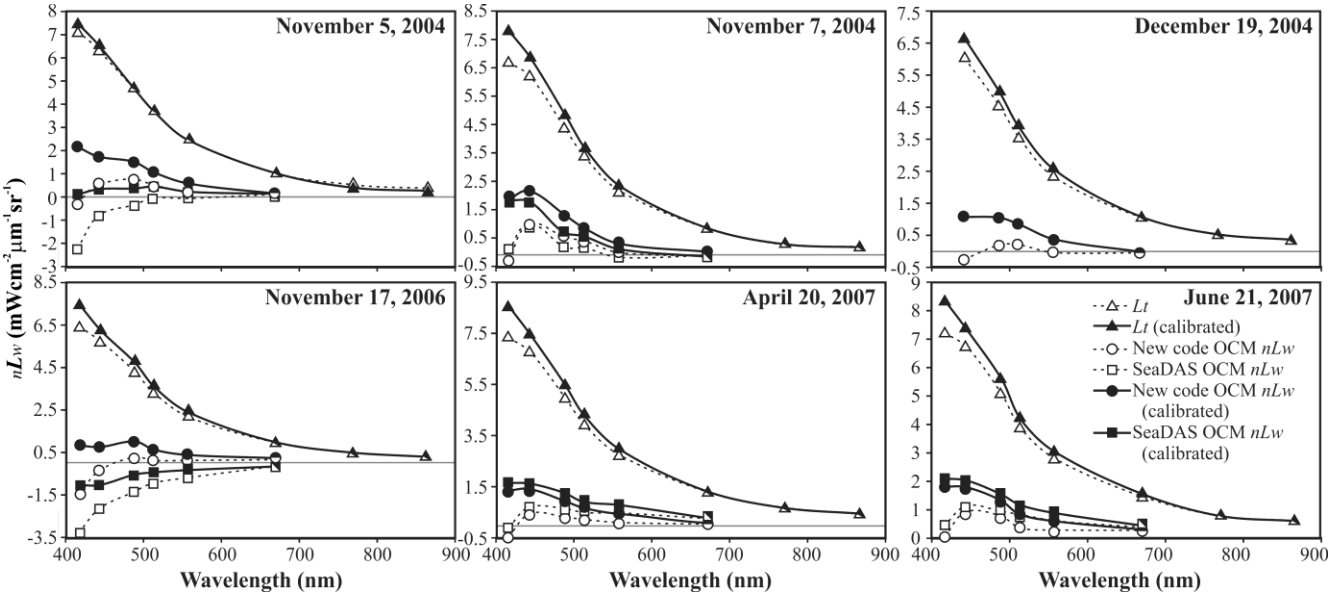

Figure 8. Comparison of new code and SeaDAS computed OCM and SeaWiFS ${}_nL_w$.

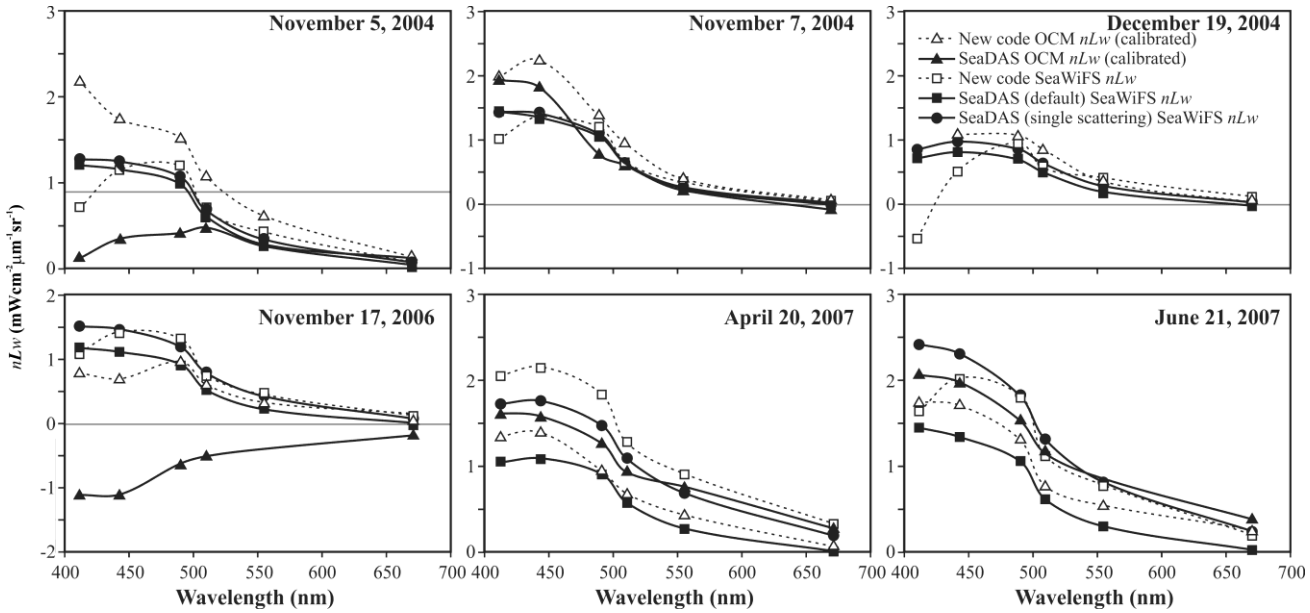

The new code and SeaDAS computed vicariously calibrated OCM ${}_nL_w$ spectra were in good agreement with each other for the most part except for 5 November, 2004, when a difference in the first three bands was observed, and for 17 November, 2006, when the SeaDAS processed spectra were negative for all the bands. The new code processed OCM spectral shapes for these two dates were in good agreement with SeaDAS processed SeaWiFS (both single and multi-scattering) and the new code processed SeaWiFS results, but the SeaDAS processed OCM spectra were not in agreement with any other spectral shapes. In fact, there was maximum disagreement on these two dates between the SeaDAS and new code computed L_r (Figure 6). Therefore, it can be concluded that on these two dates

and probably on 19 December 2004 when maximum disagreement between the SeaDAS and new code computed L_r was observed, the new code computed L_r values were more realistic compared to SeaDAS computed L_r. It is because the new code computed ${}_nL_w$ values were in agreement with SeaWiFS ${}_nL_w$ (Figure 8). Thus, the new code provided SeaWiFS-like ${}_nL_w$ values.

Figure 9. Comparison of TOA radiance before vicarious calibration (L_t) and after vicarious calibration (Calibrated L_t) at four selected sites (S1, S7, S9 and S12) from the 12 sites in Lac des Allemands for the OCM data of 20 April 2007. Comparison of Rayleigh path radiance (L_r) calculated by the new code and SeaDAS at these 4 sites is also shown.

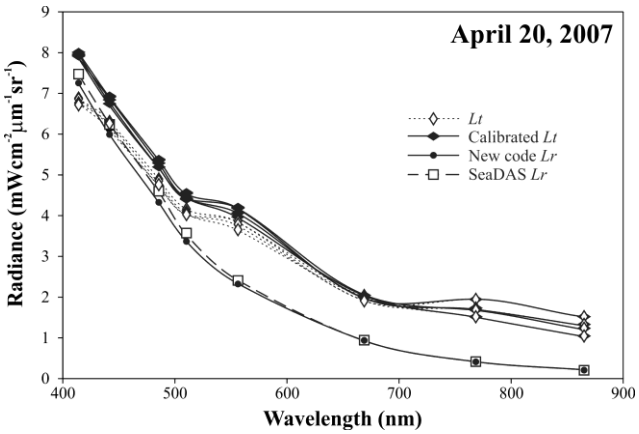

Figure 10. Comparison of aerosol radiance (L_a) calculated by the new code and SeaDAS at the 12 sites in Lac des Allemands for the OCM data of 20 April 2007.

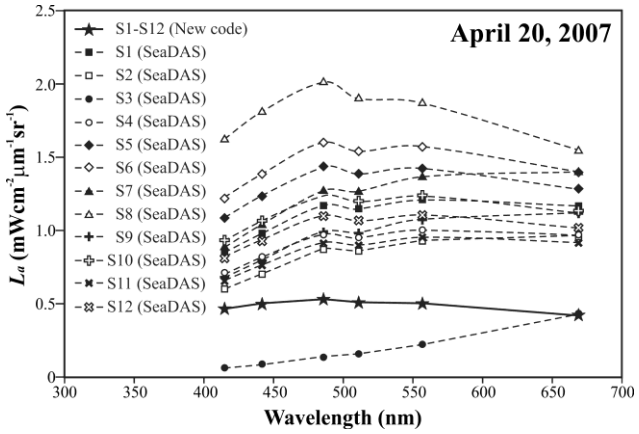

In summary, we have demonstrated that an accurate atmospheric correction of OCM data is possible using our modified atmospheric correction procedure. Using the calibration coefficients determined from the clear-water locations, realistic ${}_nL_w$ values could be obtained from OCM data. This atmospheric correction procedure was applied to all our clear-sky OCM data covering Lac des Allemands. Figure 9 shows the TOA radiances from OCM data of 20 April 2007 at four selected sites in the lake before and after vicarious calibration, along with comparisons of the Rayleigh radiances calculated by the new code and SeaDAS. Before the vicarious calibration, negative ${}_nL_w$ values were computed by both new code and SeaDAS in OCM bands 1 and 2 because the TOA radiances were less than Rayleigh radiances at those bands. As Lac des Allemands is a very small lake, there is not much variation in the viewing and solar angles and atmospheric pressure, therefore, both the new code and

SeaDAS calculated Rayleigh radiances were similar for all the sites. Fortuitously, Lac des Allemands falls on the scene center and the OCM sensor has an exact repeat coverage. Therefore, L_r computations by new code for all the other dates were as accurate as L_r shown in Figure 9. A comparison of aerosol radiances computed by the new code and SeaDAS at the 12 sites is presented in Figure 10. Our L_a estimation scheme used the Hu *et al.* [11] technique, which "borrows" aerosol types of an adjacent clear-water region to apply over turbid Case 2 waters. Assuming the aerosol characteristics do not change over short distances, we transferred the aerosol characteristics from a clear-water pixel and applied it to all 12 sites in Lac des Allemands. In contrast, SeaDAS uses an iterative approach that assumes a "known" empirical relationship between the L_w values for at least three bands (usually bands 6, 7, and 8) and chlorophyll *a*. However, in a hyper-eutrophic lake such as Lac des Allemands, the results of the empirical relationships could be erroneous. Therefore, the iterative approach produces errors in computed L_a. In such a small lake, it is unrealistic to have such a large range of aerosol radiance as shown by the SeaDAS computed L_a values at the 12 sites (Figure 10). The large range is likely attributable to variations in water constituents rather than variations in aerosol characteristics.

Due to variations in relative response of the individual detectors on the CCD array, OCM radiance images sometimes have along-track stripes especially obvious in OCM bands 1, 2, and 3 [36]. Figure 11 shows the comparison of R_{rs} obtained from *in situ* measurements and R_{rs} estimated by the new code before and after destriping for 21 June and 11 October 2007 at a central lake site. Clearly, destriping improved the R_{rs} spectra and reduced the abnormalities in the blue bands. The destriping smoothed out the noise from bad detectors and the destriped OCM R_{rs} spectra matched closely with the *in situ* radiometer spectra. The high closure between the radiometer R_{rs} and the new code R_{rs} demonstrated the effectiveness of the procedures developed in this study.

Figure 11. Comparison of *in situ* R_{rs} and R_{rs} estimated by the new code before and after destriping. *In situ* R_{rs} was obtained with a hand-held hyperspectral radiometer and then weighted with the relative spectral response function of each OCM band.

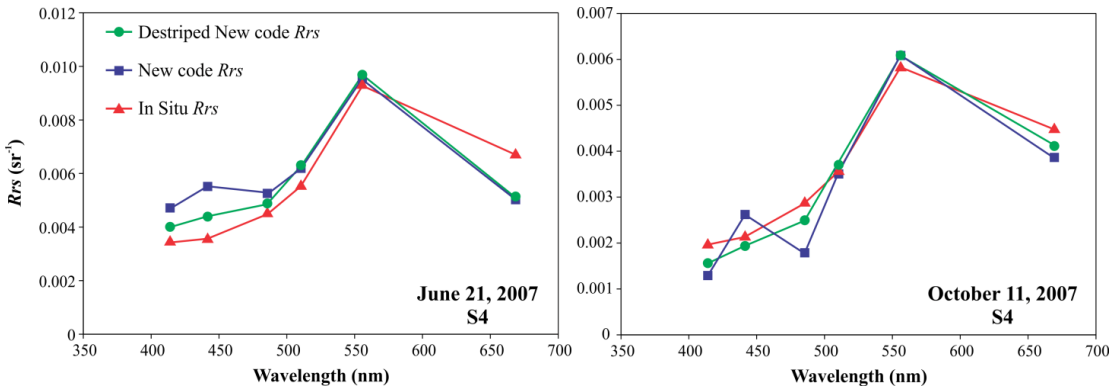

Comparison of ${}_nL_w$ calculated by SeaDAS and the new code before and after destriping of OCM data at five selected sites in the lake is shown in Figure 12. Since SeaDAS yielded slightly higher L_a, the SeaDAS processed ${}_nL_w$ values are negative in the first four bands (Figure 12(A)). For one site, S3, the SeaDAS computed ${}_nL_w$ values were positive and highest among all the sites. S3 is located in southwest Lac des Allemands, where a bayou introduces copious amounts of suspended sediments and dissolved material from surrounding areas to the lake. On 20 April 2007 the water color at S3 was

brown to dark brown as observed visually during the field trip and also in the OCM "true color" image (Figure 13). Measured *in situ* data suggested a CDOM absorption coefficient of 13.05 m^{-1} (at 412 nm), a SPM concentration of 12 mg/L and a chlorophyll *a* concentration of 36.72 µg/L at that site on 20 April 2007. As SPM was found to be relatively dark detrital matter at S3 and CDOM exhibits high absorption in the blue bands, there should be more absorption especially in the blue and therefore ${}_nL_w$ should be lower than other sites. Hence, the relatively high ${}_nL_w$ computed by SeaDAS for the OCM data at S3 seems unrealistic. In contrast, the new code computed ${}_nL_w$ values were positive throughout the visible spectrum (Figure 12(B,C)). For S3, the lowest ${}_nL_w$ was observed as expected. In Figure 12(B), the remaining imperfections were due to striping. After destriping (Figure 12(C)), the new code computed ${}_nL_w$ spectra resembled the ideal phytoplankton spectra [39]. By employing this combined atmospheric correction and vicarious calibration procedure more accurate R_{rs} values were obtained from all our OCM data. In fact, very realistic R_{rs} values were retrieved over the entire Lac des Allemands. An example showing the R_{rs} spectra of all the 572 pixels in Lac des Allemands for 20 April 2007 is presented in Figure 13(A) together with the band 5 OCM image of 20 April 2007 for the identification of those 572 pixels and the corresponding true color image in Figure 13(B,C), respectively. This shows the effectiveness of the procedure developed in this study. Using the R_{rs} values retrieved for nine dates during 2006–2007, new algorithms were successfully developed for estimating cyanobacteria by quantifying phycocyanin and chlorophyll *a* in Lac des Allemands [3].

Figure 12. Comparison of normalized water-leaving radiance (${}_nL_w$) calculated by SeaDAS and by the new code before and after destriping of the OCM data of 20 April 2007 at selected 5 sites (S1, S3, S7, S9 and S12) out of the 12 sites in Lac des Allemands.

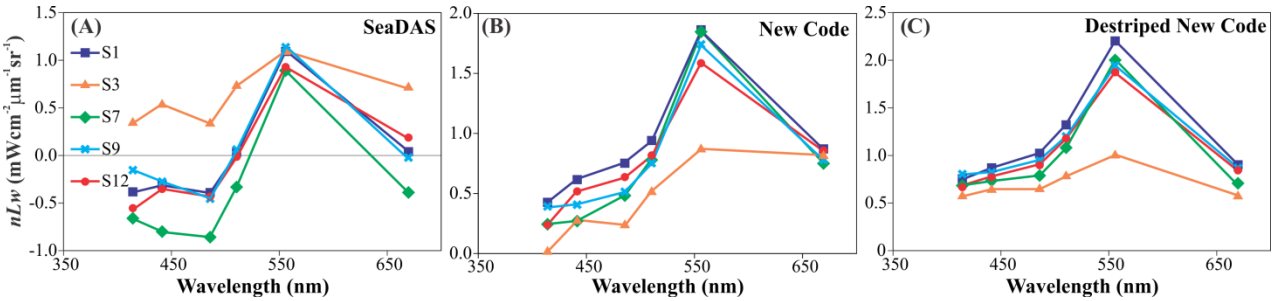

Retrieval of accurate R_{rs} in coastal Case 2 waters provides a challenge for satellite remote sensing [40–42]. The standard atmospheric correction procedure developed for SeaWiFS yields unacceptable errors, and/or masks the Case 2 water pixels due to atmospheric correction failure. The atmospheric correction procedure presented here reduces errors in the estimated water-leaving radiance and provides more accurate results in small- to moderate-sized coastal water bodies. The accuracy in the estimated water-leaving radiance may sometimes exhibit minor errors due to the use of a single scattering approximation (if the site is located towards the scan edge) or due to the homogeneous aerosol assumption. Nevertheless, the simple atmospheric correction procedure described here can be used to obtain improved retrievals in Case 2 waters and can be easily modified based on user needs. A vicarious calibration procedure was also developed for the recalibration of OCM data. For two sensors having identical bands and similar overpass times, vicarious calibration coefficients can be derived for one sensor using ${}_nL_w$ values from the well-calibrated sensor over clear-water locations by following

this procedure. In the absence of *in situ* ${}_nL_w$ data, this procedure is a cost effective solution for the vicarious calibration of any ocean color sensor.

Figure 13. (**A**) R_{rs} spectra of all the 572 pixels in Lac des Allemands for 20 April 2007. (**B**) The 572 pixels have been identified in the band 5 OCM image. (**C**) Twelve sampling sites (S1-S12) are indicated in the true color OCM image.

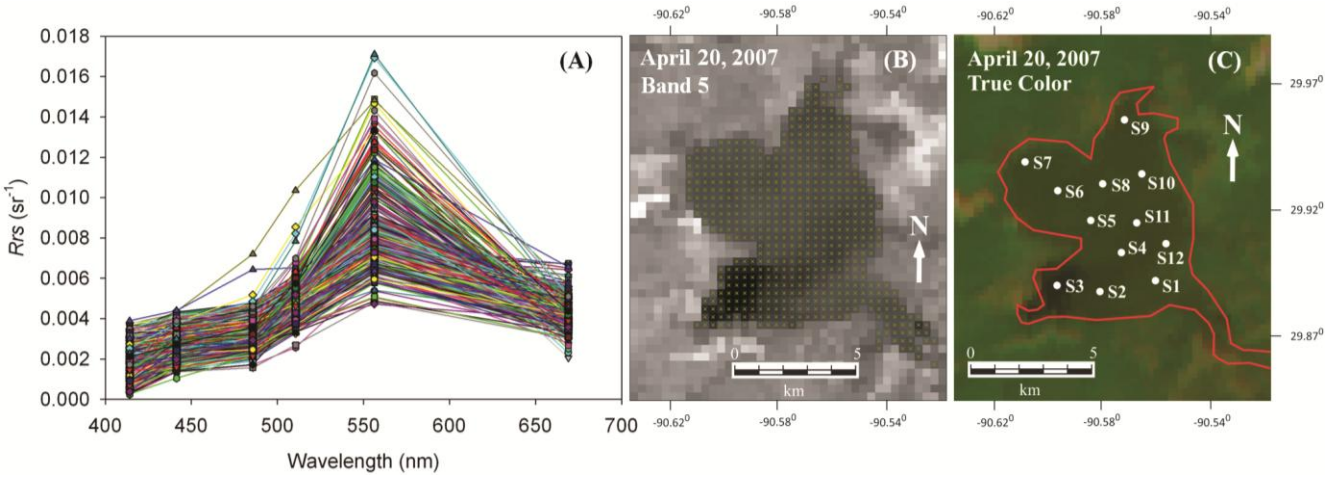

4. Conclusions

This paper presents a detailed methodology for the atmospheric correction of Oceansat-1 Ocean Color Monitor (OCM) data, an ocean color sensor that provides visible and near-infrared measurements at high resolution (240 × 360 m pixels) in the same 8 wavelength regions as the well-known NASA SeaWiFS sensor with a 1 × 1 km spatial resolution. The ultimate motivation for this work was to quantify cyanobacterial pigments by satellite within a small brackish/freshwater lake in coastal Louisiana, USA, where toxic cyanobacterial blooms occur frequently. At the outset of this research, a functional atmospheric correction procedure for OCM data was not available to researchers. In addition, OCM calibration coefficient updates were not provided to the user community regularly, requiring a vicarious calibration between sensors, which was performed using SeaWiFS as a reference. The Case 2 water study area required modification of the standard NASA Case 1 aerosol correction technique, which is invalid in this optically complex lake due to the high concentrations of chromophoric dissolved organic matter and organic/inorganic sediments in additional to algal pigments.

Over Case 1 clear water locations, the ${}_nL_w$ values from OCM data computed by the combined atmospheric correction and vicarious calibration procedure developed in this study were very similar to the normalized water leaving radiance (${}_nL_w$) values provided by SeaWiFS Data Analysis System (SeaDAS) software package from SeaWiFS and OCM data. The remote sensing reflectance (R_{rs}) obtained after the atmospheric correction of OCM data over the lake were in good agreement with *in situ* R_{rs}, and the spectral shapes resembled chlorophyll *a* rich Case 2 waters, while SeaDAS and other atmospheric correction procedures produced either negative or erroneous ${}_nL_w$ values or masked all pixels in the small lake. These improved ${}_nL_w$ or R_{rs} retrievals allowed for more accurate estimates of algal pigments in a brackish, freshwater lake southwest of New Orleans, Louisiana, USA.

SeaDAS was developed over many years with an emphasis on retrieving chlorophyll *a* in Case 1 waters. Many researchers have tried to use SeaDAS processed data in coastal waters where the atmospheric correction procedure developed for Case 1 waters does not work. This paper presents a straight forward approach for atmospheric correction which can be used by researchers to retrieve better results in coastal waters. The method developed and described in detail here can be applied to the recently launched OCM-2 sensor and other sensors including Moderate Resolution Imaging Spectroradiometer (MODIS), QuickBird, and the Visible Infrared Imager Radiometric Suite (VIIRS). Future research would benefit from *in situ* validation experiments in a range of Case 2 environments potentially with different aerosol characteristics, to further assess the applicability of this atmospheric correction procedure.

Acknowledgments

This work was funded by National Aeronautics and Space Administration (NASA) grant HBCU NCC13-03001 through the Southern University Center for Coastal Zone Assessment and Remote Sensing Program, as well as a grant from Shell NGI project. The authors are thankful to Chuanmin Hu, University of South Florida, for his help in atmospheric correction. The authors thank Bryan Franz, NASA Goddard Space Flight Center, for incorporating OCM data processing capabilities in SeaDAS, and the OBPG team at NASA Goddard Space Flight Center for providing support and answering questions on SeaDAS. We thank Alaric Haag and Chet Pilley for their help with the Terascan™ software, and Mary Lee Eggart, Dr. Puneeta Naik and Hiranya Sahoo for aiding with the figures. SeaWiFS data are the property of GeoEye Corp. and its use here is in accordance with the SeaWiFS research data use terms and conditions agreement of the NASA SeaWiFS project.

References

1. Gould, R.W.; Arnone, R.A. Remote sensing estimates of inherent optical properties in a coastal environment. *Remote Sens. Environ.* **1997**, *61*, 290–301.
2. Morel, A.; Prieur L. Analysis of variations in ocean color. *Limnol. Oceanogr*. **1977**, *22*, 709–722.
3. Dash, P.; Walker, N.D.; Mishra, D.R.; Hu, C.; Pinckney, J.L.; D'Sa, E.J. Estimation of cyanobacterial pigments in a freshwater lake using OCM satellite data. *Remote Sens. Environ.* **2011**, *115*, 3409–3423.
4. Garcia, A.C.; Bargu, S.; Dash, P.; Rabalais, N.N.; Sutor, M.; Morrison, W.; Walker, N.D. Evaluating the potential risk of microcystins to blue crab (*Callinectes sapidus*) fisheries and human health in a eutrophic estuary. *Harmful Algae* **2010**, *9*, 134–143.
5. Ren, L.; Rabalais, N.N.; Morrison, W.; Mendenhall, W.; Turner, R.E. Nutrient limitation on phytoplankton growth in upper Barataria Basin, Louisiana: microcosm bioassays. *Estuaries Coasts* **2009**, *32*, 958–974.
6. Kutser, T. Passive optical remote sensing of cyanobacteria and other intense phytoplankton blooms in coastal and inland waters. *Int. J. Remote Sens.* **2009**, *30*, 4401–4425.
7. Hooker, S.B.; McClain, C.R.; Holmes, A. Ocean color imaging: CZCS to SeaWiFS. *Marine Technol. Soc.* **1993**, *27*, 2–15.

8. O'Reilly, J.E.; Maritorena, S.; Mitchell, G.G.; Siegel, D.A.; Carder, K.L.; Garver, S.A.; Kahru, M.; McClain, C. Ocean color algorithms for SeaWiFS. *J. Geophys. Res.* **1998**, *103*, 24937–24953.
9. Crowley, M.F.; Bernstein, R.; Prasad, K.; Glenn, S. Oceansat's Ocean Color Monitor: An Instrument Whose Time Has Come. *In Proceedings of Oceans 2003*, San Diego, CA, USA, 22–26 September 2003; Volume 3, pp. 1581.
10. ISRO. Oceansat-2 Meeting Global Demand. *In Proceedings of 53rd Session of UNCOPUS 2010*, Vienna, Austria, 9–18 June 2010; p. 11.
11. Hu, C.; Carder, K.L.; Muller-Karger, F.E. Atmospheric correction of SeaWiFS imagery of turbid coastal waters: A practical method. *Remote Sens. Environ.* **2000**, *74*, 195–206.
12. Wang, M.; Franz, B.A. Comparing the ocean color measurements between MOS and SeaWiFS: A vicarious intercalibration approach for MOS. *IEEE Trans. Geosci. Remote Sens.* **2000**, *38*, 184–197.
13. D'Sa, E.J.; Hu, C.; Muller-Karger, F.E.; Carder, K.L. Estimation of colored dissolved organic matter and salinity fields in case 2 waters using SeaWiFS: Examples from Florida Bay and Florida Shelf. *Proc. Indian Acad. Sci.* (*Earth Planet. Sci.*) **2002**, *106*, 197–207.
14. Arnone, R.A.; Martinolich, P.; Gould, R.W., Jr.; Stumpf, R.P.; Ladner, S. Coastal Optical Properties Using SeaWiFS. *In Proceedings of Ocean Optics XIV 1998*, Kailua Kona, HI, USA, 10–13 November 1998.
15. Stumpf, R.P.; Arnone, R.A.; Gould, R.W.Jr.; Martinolich, P.M.; Ransibrahmanakul, V. A Partially Coupled Ocean-Atmosphere Model for Retrieval of Water-Leaving Radiance from SeaWiFS in Coastal Waters. In *Algorithm Updates for the Fourth SeaWiFS Data Processing. SeaWiFS Postlaunch Technical Report Series*; Hooker, S.B., Firestone E.R., Eds.; NASA Goddard Space Flight Center: Greenbelt, MD, USA, 2003; Volume 22, pp. 51–59.
16. Siegel, D.A.; Wang, M.; Maritorena, S.; Robinson, W. Atmospheric correction of satellite ocean color imagery: The black pixel assumption. *Appl. Opt.* **2000**, *39*, 3582–3591.
17. Gordon, H.R. Atmospheric correction of ocean color imagery in the Earth Observing System era. *J. Geophys. Res.* **1997**, *102*, 17081–17106.
18. Hu, C.; Chen, Z.; Clayton, T.D.; Swarzenski, P.; Brock, J.C.; Muller-Karger, F.E. Assessment of estuarine water-quality indicators using MODIS medium-resolution bands: Initial results from Tampa Bay, FL. *Remote Sens. Environ.* **2004**, *93*, 423–441.
19. Franz, B.A.; Bailey, S.W.; Werdell, P.J.; McClain, C.R. Sensor-independent approach to the vicarious calibration of satellite ocean color radiometry. *Appl. Opt.* **2007**, *46*, 5068–5082.
20. McClain, C.R.; Ainsworth, E.J.; Barnes, R.A.; Eplee, R.E.; Patt, F.S.; Robinson, W.D.; Wang, M.; Bailey, S.W. SeaWiFS Postlaunch Calibration and Validation Overview. In *SeaWiFS Postlaunch Calibration and Validation Analyses*; Hooker S.B., Firestone E.R., Eds.; NASA Goddard Space Flight Center: Greenbelt, MD, USA, 2000; pp. 4–11.
21. Barnes, R.A.; Eplee, R.E.; Schmidt, G.M.; Patt, F.S.; McClain, C.R. The calibration of SeaWiFS. I direct techniques. *Appl. Opt.* **2001**, *40*, 6682–6700.
22. Eplee, R.E.; Robinson, W.D.; Bailey, S.W.; Clark, D.K.; Werdell, P.J.; Wang, M.; Barnes, R.A.; Mcclain, C.R. The calibration of SeaWiFS. II vicarious techniques, *Appl. Opt.* **2001**, *40*, 6701–6718.

23. Suresh, T.; Desa, E.; Mascarenhas, A.; Matondkar, S.G.P.; Naik, P.; Nayak S.R. Cross Calibration of IRS-P4 OCM Satellite Sensor. *In Proceedings of SPIE*, Goa, India, 13–17 November 2006; Volume 6404, pp. 1–9.
24. Gordon, H.R.; Clark, D.K.; Brown, J.W.; Brown, O.B.; Evans, R.; Broenkow, W.W. Phytoplankton pigment concentrations in the Middle Atlantic Bight: Comparison of ship determinations and CZCS estimates. *Appl. Opt.* **1983**, *22*, 1, 20–36.
25. Mishra, D.R.; Narumalani, S.; Rundquist, D.; Lawson, M. High-Resolution ocean color remote sensing of benthic habitats: A case study at the Roatan Island, Honduras. *IEEE Trans. Geosci. Remote Sens.* **2005**, *43*, 1592–1604.
26. Gordon H.R. Remote sensing of ocean color: a methodology for dealing with broad spectral bands and significant out-of-band response. *Appl. Opt.* **1995**, *34*, 8363–8374.
27. Gregg, W.W.; Carder, K.L. A simple spectral solar irradiance model for cloudless maritime atmospheres. *Limnol. Oceanogr.* **1990**, *35*, 1657–1675.
28. Pandya M.R.; Singh, R.P.; Murali, K.R.; Babu, P.N.; Kirankumar A.S.; Dadhwal, B.K. Bandpass Solar Exoatmospheric Irradiance and Rayleigh Optical Thickness of Sensors On Board Indian Remote Sensing Satellites-1B, -1C, -1D, and P4. *IEEE Trans. Geosci. Remote Sens.* **2002**, *40*, 714–718.
29. Hansen J.E.; Travis L.D. Light scattering in planetary atmospheres. *Space Sci. Rev.* **1974**, *16*, 527–610.
30. Doerffer, R. Imaging Spectroscopy for Detection of Chlorophyll and Suspended Matter. In *Imaging Spectroscopy: Fundamentals and Prospective Applications*; Toselli, F., Bodechtel, J., Eds.; Kluwer: London, UK, 1992; pp. 215–257.
31. Bailey, S.; Franz, B. Personal Communication. 21 October 2009.
32. Gordon, H.R.; Wang, M.H. Retrieval of water-leaving radiance and aerosol optical-thickness over the oceans with Seawifs—A preliminary algorithm. *Appl. Opt.* **1994**, *33*, 443–452.
33. Mohan, M.; Chauhan, P. *Atmospheric Correction for Ocean Color Remote Sensing*, *ISRO Scientific Report*; IRS-P4/SATCORE/SAC/RESIPA/MWRG/SR/22/2003; ISRO: Ahmedabad, India, 2003; p. 22.
34. Gordon, H.R.; Voss, K.J. *Modis Normalized Water-Leaving Radiance Algorithm Theoretical Basis Document*; Contract Number NAS5-31363; NASA Goddard Space Flight Center: Greenbelt, MD, USA, 1999; pp. 1–2.
35. Kumar, S.A. Personal Communication. 3 March 2009.
36. Lyon, P.E. An automated de-striping algorithm for Ocean Color Monitor imagery. *Int. J. Remote Sens.* **2009**, *30*, 1493–1502.
37. Gordon, H.R.; Brown, J.W.; Evans, R. Exact Rayleigh scattering calculations for use with the Nimbus-7 Coastal Zone Color Scanner. *Appl. Opt.* **1988**, *27*, 862–871.
38. Kattawar, G.W.; Plass, G.N.; Hitzfelder, S.J. Multiple scattered radiation emerging from Rayleigh and continental haze layers. 1: Radiance, polarization, and neural points. *Appl. Opt.* **1976**, *15*, 632.
39. Wang, M.H., Ed. *Atmospheric Correction for Remotely-Sensed Ocean-Colour Products*; Reports of the International Ocean-Colour Coordinating Group; IOCCG: Dartmouth, Canada, 2010; Volume 10, p. 78.

40. Sokoletsky, L.G.; Lunetta, R.S.; Wetz, M.S.; Paerl, H.W. MERIS retrieval of water quality components in the turbid albemarle-pamlico sound estuary, USA. *Remote Sens.* **2011**, *3*, 684–707.
41. Chen, H.-W.; Cheng, K.-S. A Conceptual model of surface reflectance estimation for satellite remote sensing images using *in situ* reference data. *Remote Sens.* **2012**, *4*, 934–949.
42. Bagheri, S. Nearshore Water quality estimation using atmospherically corrected AVIRIS data. *Remote Sens.* **2011**, *3*, 257–269.